Full length article

Nanofabrication, characterisation and modelling of soft-in-hard FeCo–FePt magnetic nanocomposites

Isabelle G. de Moraes [a,b,*], Johann Fischbacher [c], Yuan Hong [a,**], Cécile Naud [a], Hanako Okuno [d], Aurelien Masseboeuf [b], Thibaut Devillers [a], Thomas Schrefl [c], Nora M. Dempsey [a]

[a] Univ. Grenoble Alpes, CNRS, Grenoble INP, Institut NEEL, Grenoble, 38000, France
[b] Univ. Grenoble Alpes, CEA, CNRS, Grenoble INP, IRIG-Spintec, Grenoble, 38000, France
[c] Christian Doppler Laboratory for magnet design through physics informed machine learning, Department for Integrated Sensor Systems University for Continuing Education Krems, Wiener Neustadt, 2700, Austria
[d] Univ. Grenoble Alpes, CEA, CNRS, Grenoble INP, IRIG-MEM, Grenoble, 38000, France

ARTICLE INFO

ABSTRACT

Advanced nanofabrication exploiting e-beam lithography has been used to prepare nanocomposites consisting of periodic arrays of soft magnetic FeCo-based nano-inclusions of variable dimensions, embedded in a hard magnetic FePt matrix. Nanocomposites with non-magnetic (Pt) inclusions and single phase hard magnetic FePt microstructures were prepared as reference samples. The formation of Kirkendall voids in the soft-in-hard nanocomposites, because of annealing-induced diffusion, has been identified through high resolution imaging and chemical analysis. Replication of the μm-scaled nanocomposite and hard magnetic units over mm-scaled surfaces allowed global magnetic characterisation of magnetisation reversal using standard magnetometry. Magnetic force microscopy imaging was used for spatially resolved magnetic characterisation in different remanent magnetic states. Both of these experimental techniques were used to study the influence of the size, volume content and nature of the nano-inclusions on magnetisation reversal. The well-defined geometry and nano-scaled size of the inclusions render these nanocomposites as model systems for micromagnetic simulations and very good agreement was achieved between measured and simulated magnetisation reversal curves. This accordance motivates future in-silico optimisation of such soft-in-hard nanocomposites, which may serve as model systems to guide the design of new high performance bulk magnets which are less dependent on critical elements.

1. Introduction

The discovery that Fe-rich Nd-Fe-B alloys produced by melt-spinning show remanence enhancement [1] opened the field of hard–soft nanocomposites, and the effect was subsequently explained by the concept of exchange-spring magnets [2]. The essential idea consists in combining the high magnetisation of a soft magnetic phase with the high anisotropy of a hard magnetic phase, so as to produce a magnet with an energy product $(BH)_{max}$ exceeding that of one based on the hard phase alone. Interest in this class of magnetic materials has been renewed as they offer the potential to reduce the content of strategic and expensive elements used to make high performance magnets (rare earths such as Nd, Pr, and Sm, as well as Pt and Pd). Micromagnetic simulations predicted room temperature energy products of 800 kJ/m³ for a $SmCo_5/\alpha$-Fe multilayer with 85 vol% soft phase [3] and a record value of 1 MJ/m³ for a $Sm_2Fe_{17}N_3/Fe_{65}Co_{35}$ multilayer with almost 80 vol% soft phase [4]. Nanocomposite magnets with a more complex sample architecture consisting of building blocks with a soft core ($Fe_{65}Co_{35}$), hard matrix ($Nd_2Fe_{14}B$) and super-hard grain-shell ($Sm_2Fe_{17}N_3$) have been predicted to have an energy product greater than 400 kJ/m³ at the application relevant temperature of 450 K, for a 40 vol.% soft phase content [5]. However, to achieve the predicted excellent magnetic properties in real magnets, it is necessary to have nanoscale control of the soft phase dimensions, sharp chemical interfaces and strong exchange coupling between the phases.

The routes that have been used to fabricate hard–soft nanocomposites can be categorised into three groups: chemical, metallurgical and thin film deposition. Chemical routes based on nanoparticle preparation, in which the soft and hard phases are intimately mixed through core–shell structuration [6] and self-assembly [7], have been used to

---

* Corresponding author at: Univ. Grenoble Alpes, CNRS, Grenoble INP, Institut NEEL, Grenoble, 38000, France.
** Corresponding author.
E-mail addresses: isabelle.gomesdemoraes@cea.fr (I.G. de Moraes), yuan.hong@neel.cnrs.fr (Y. Hong).

fabricate ferrite, FePt and SmCo [8] based nanocomposites [9]. Metallurgical routes [10] used to produce nanostructured powders include melt-spinning and high energy ball milling [11]. The relatively low coercivity generally reported for chemically and metallurgically prepared nanocomposites are attributed to insufficient control of the soft-phase dimensions [12]. However, there have been some very promising recent reports on the development of anisotropic nanocomposite powders with relatively high coercivity, either by chemical coating of FeCo onto the surface of $SmCo_5$ flakes produced by surfactant-assisted ball milling [13], or application of a modified hydrogenation disproportionation desorption recombination (HDDR) process to produce $Nd-Fe-B/\alpha-Fe$ [14]. While chemical and metallurgical routes hold potential for the manufacture of bulk nanocomposite magnets for use at the macroscale, the application of patterned thin film nanocomposites is necessarily limited to micro- or nano-devices. However, thin films are of great interest as model systems to study magnetisation reversal in hard–soft nanocomposites, owing to the greater degree of control achievable over the nano-structure. Multilayered hard–soft structures comprised of various combinations of different materials such as $Nd_2Fe_{14}B/Fe$ [15], $SmCo_5/Co$ [16], $SmCo_5/Fe$ [17] and FePt/Fe [18] have been studied. The achievement of texture in the hard phase favours high energy products and a maximum value of 400 kJ/m^3 was reported in a fully epitaxial $SmCo_5/Fe/SmCo_5$ trilayer deposited by Pulsed Laser Deposition (PLD) [19]. In some multilayer based studies, a spacer layer has been used to avoid diffusion and to tune exchange interactions between the hard and soft phases [20]. In-plane patterning adds an additional degree of control over the nanostructure of films. Nanoimprint lithography with a commercial Si stamp combined with etching was used to fabricate mm-sized arrays of FePt/Co bilayer nanomagnets of fixed diameter (60 nm), in which the thickness of the hard phase was also fixed (20 nm) while the thickness of the soft phase was varied (0, 1 and 4 nm). Coercivity dropped and magnetisation increased as the soft layer thickness increased, and the loop shape switched from 1-phase behaviour (fully exchange coupled) to 2-phase behaviour (partially exchange coupled) as the soft phase thickness increased from 1 nm to 4 nm [21,22].

In this work we exploit the high spatial resolution and dimensional tunability of e-beam lithography to prepare model hard–soft nanocomposites consisting of arrays of soft magnetic FeCo nano-inclusions embedded in a hard-magnetic matrix of $L1_0$ FePt. This "soft-in-hard" architecture was chosen based on theoretical modelling by Skomski et al. which suggested that soft-in-hard structures should have higher coercivities than hard-in-soft structures [23]. We explore the influence of the size and volume content of as-prepared soft nano-rods on the nanocomposites' magnetic properties, experimentally using magnetometry, and theoretically, using micromagnetic simulations. In contrast with studies of chemically or metallurgically prepared nanocomposites, the control we achieve over the dimensions and spatial distribution of soft inclusions minimises the differences between the physical nanostructure that we experimentally probe and the idealised nanostructure that we model.

2. Experimental and simulation details

The process-flow developed to make hard–soft nanocomposites is schematised in Fig. 1. The soft magnetic component was fabricated using e-beam lithography, thin film deposition and lift-off (Top part of Fig. 1). The substrates used were 2-inch Si wafers thermally oxidised to a depth of 100 nm. Deposition of a Ta buffer layer by magnetron sputtering was followed by spin coating of a resist layer (55 nm - poly(methyl methacrylate)(PMMA) 2%) which was then exposed to an electron beam (NBL Nanobeam) and developed with methyl isobutyl ketone(MIBK)/isopropyl alcohol (IPA) (1:3). Deposition of a 10 nm thick layer of FeCo coated with a 3 nm thick protective layer of Au was performed using an e-gun evaporator (Plassys). Lift-off was then performed to produce the nano-rods, using N-methyl-2-pyrrolidone (NMP)

as solvent. To provide enough magnetic signal for global magnetometry measurements, nano-rod array units of surface area 5×5 μm^2 were replicated over a surface area of 3×2 mm^2 (bottom part Fig. 1). The replication procedure was used as the surface area that can be patterned with a high density of nano-structures by e-beam lithography is limited to a few μm because of the proximity effect [24]. Following extensive optimisation of the resist thickness and e-beam dose, the above described procedure was used to fabricate the soft magnetic inclusions of the final nanocomposite.

The hard magnetic matrix ($L1_0$ FePt) was fabricated using magnetron sputtering (FePt films of thickness 25 nm, covered with a Ta capping layer of thickness 5 nm) at room temperature followed by post-deposition annealing. The composition of the FePt film and the annealing temperature used to form the ordered $L1_0$ phase were optimised through a prior study of compositionally graded Fe-Pt films [25]. An X-ray diffraction pattern and M-H loops of a reference FePt film prepared under the same conditions are shown in the Supplementary material (Fig. S1), confirming the formation of randomly oriented grains of the $L1_0$ phase. A second "layer" of e-beam lithography and lift-off were used to micro-pattern the as-deposited FePt film into so-called "μ-pads", exclusively covering of the nano-rod arrays (lower part Fig. 1). In this case, a bi-layer resist (PMMA 2% and PMMA/Methyl methacrylate (MMA) 3%) was used to form an undercut profile to allow lift-off of the sputtered FePt film. These micro-patterned substrates containing arrays of soft nano-rods were transferred to the magnetron sputtering system and the Au capping layer of the nano-rods was etched off just before deposition of the FePt/Ta bi-layer. Following removal of the sample from the sputtering system and lift-off of the resist to form μ-pads, annealing of the assembled nanocomposite was carried out at 500 °C during 1 h in a tube furnace under secondary vacuum (10^{-8} mbar). The same process was used to fabricate a nanocomposite with non-magnetic nano-rods, in which the FeCo was replaced by Pt. The full set of nanocomposite samples studied in this work is listed in Table 1. Hard FePt μ-pads with no nano-rod inclusions were also prepared as reference samples.

Samples were imaged at different stages of fabrication using a Field Emission Scanning Electron Microscope (FESEM Zeiss Ultra) operated in In-Lens and Secondary Electron (SE) modes and Transmission Electron Microscopy (TEM) (CM300-Philips and a Titan Themis perated @200 kV and equipped with a Super-X detector system for Energy-Dispersive X-ray (EDX) spectroscopy). Sample preparation for TEM imaging was carried out using both polishing and a Focused Ion Beam (FIB) (Zeiss NVISION). Magnetic hysteresis loops which characterised the global magnetic response of the nanocomposites were measured using a Superconducting Quantum Interference Device-Vibrating Sample Magnetometer (SQUID-VSM) (MPMS3 Quantum Design), in maximum applied field of 6 T. The localised magnetic response of the nanocomposites was probed by Magnetic Force Microscopy (MFM) using a commercial microscope (NT-MDT-NTEGRA) and in-house developed high coercivity FePt-based MFM probes. MFM imaging was carried out under zero magnetic field, on samples in the virgin state and in different states of remanent magnetisation. The latter were induced by exposure of the sample under observation to a magnetic field pulse produced by an in-house developed magnetic field source mounted directly on the MFM.

Simulations were made using a finite element micromagnetic solver optimised for parallel computation on multiple graphical processor units (GPUs). The demagnetisation curves were calculated by applying a preconditioned conjugate gradient method minimising the Gibbs free energy as presented in [26]. Energy terms due to the magnetocrystalline anisotropy energy, exchange energy, magnetostatic energy, and Zeeman energy were considered. The external field was decreased from 6 T to −6 T in steps of −1 mT applied in-plane, either parallel or perpendicular to the long axis of the nano-rods. To represent the FePt hard magnetic μ-pad, a $700 \times 1100 \times 30$ nm^3 cuboid was split in 1500 grains using the Neper software package [27,28], see Fig. 6a. The
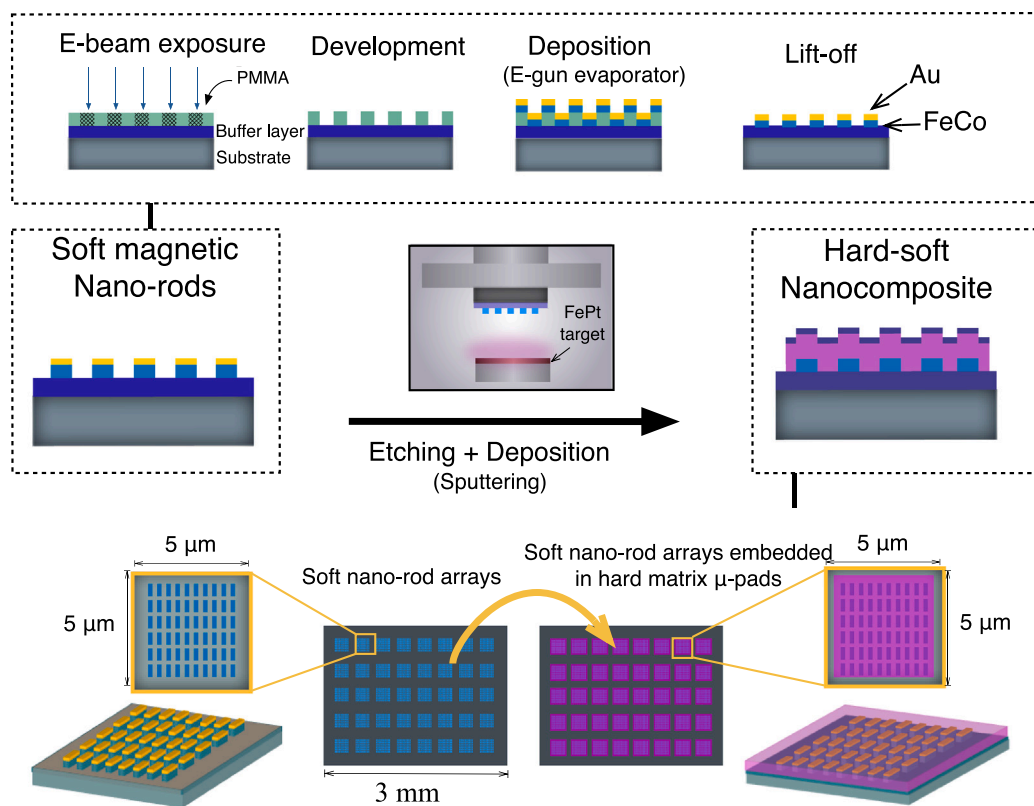
Fig. 1. Schematic of nanocomposite preparation. Top: Nano-rod array fabrication by e-beam lithography and lift-off. Bottom: Nano-rod array replication across a large surface area and coating of all arrays with hard magnetic μ-pads.

Table 1
Information about nanocomposites, according to the schematic shown in Fig. 2f.All dimensions in nm.

Sample	Nano-rod width (w)	Inter nano-rod distance (d)	Nano-rod length (l)	Soft phase volume content (%)
NC1	24	200	200	1.8
NC2	30	90	400	6.7
NC3	24	52	200	8.0
NC4	120	130	400	11.5
NC4-Pt	120	130	400	N.A.

average grain size was around 25 nm, ranging from 16 nm up to 44 nm. This model was then meshed with approximately 88 million tetrahedral elements using Salome [29] and MeshGems [30]. This number includes the finite element mesh of an air-box surrounding the hard magnetic μ-pad. Enclosing the μ-pad with an air-box is a simple method to treat the open boundary problem for magnetostatic problems [31]. For the air-box we use a graded mesh. The mesh size increases with increasing distance from the sample. The size of the cubic air-box is 11 times the lateral maximum extension of the μ-pad. The mesh size at the interfaces between grains and surfaces was set to 1.5 nm but allowing limited growth of the mesh size within the grains. This mesh was the base for all simulations. All tetrahedrons within a grain were assigned a unique tag. Those tags were then used to assign the intrinsic properties and easy axes orientations to all grains. The soft magnetic nano-rods and voids were introduced by reassigning new tags (and consequently intrinsic properties) to tetrahedrons lying within or on reference shapes representing the different nano-rod arrays. Therefore, the interfaces between rods/voids and the main matrix are not smooth. The extensions of the FePt hard magnetic μ-pad model was restricted by the available computational resources and to ease comparison was kept the same for all simulation scenarios. Consequently, the volume shares

of the soft phase differed from the experiments and were slightly higher than in the experiments (+0.4-0.6% NC1-3, +2.2% NC4).

3. Results and discussion

3.1. Micro/nano structure of as-prepared and annealed nanocomposites

Plan-view SEM images of the four different types of soft magnetic arrays are shown in Figs. 2a–d. The width (w) and length (l) of the rods, together with the inter-rod distance (d), are schematised in Fig. 2f, and the volume ratio they represent for the corresponding nanocomposites, are listed in Table 1. The smallest width of nano-rods prepared (24 nm) corresponds to the lower limit of the in-plane dimension achievable with e-beam lithography considering the high density of features produced. A tilted view image of part of the soft nano-rod array shown in Fig. 2b is presented in Fig. 2e, revealing neat lift-off (i.e., no underlying resist remaining) over this high density of nanometric structures. A plan-view image of a similar array embedded in an FePt μ-pad is shown in Fig. 2g. The underlying soft nano-rods can be visualised through the hard-magnetic μ-pad thanks to the topographic contrast achieved in the SEM Secondary Electron imaging mode. Plan-view SEM images of a reference FePt hard μ-pad and the other soft-in-hard nanocomposite (NC) samples are compared in the Supplementary materials (S2).

A TEM cross-sectional bright field image of a FIB-cut piece of the NC2 sample, taken before annealing, is shown in Fig. 3a. The FePt matrix follows the topography imposed by the underlying FeCo nano-rods. Grains of FePt of inverted-trapeze shape grow on top of the FeCo nano-rods. The FePt deposit in-between these grains is typically one, but sometimes two grains deep. Since the film thickness is comparable to the grain size, small local variations in thickness can be observed because the growth rate might differ slightly from grain to grain, depending on their orientation. The bright contrast at the interface between the Ta buffer layer and the nanocomposite layer is attributed
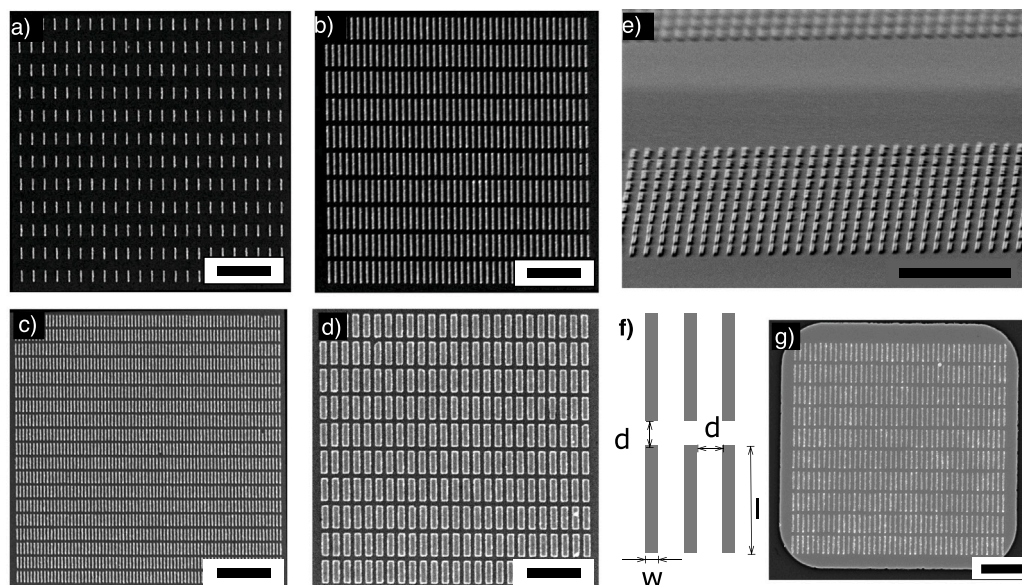
Fig. 2. Secondary electron SEM images: Plan-view images of soft nano-rod arrays prior to deposition of hard μ-pad (a) NC1, (b) NC2, (c) NC3 and (d) NC4; (e) tilted view of NC2 (nano-rod array); (g) plan-view of NC2 (soft nano-rod array embedded in an FePt μ-pad). Scale bar = 1 μm. Schematic of a nano-rod array (f).

to surface oxidation of the buffer during the substrate preparation. The bright granular contrast at the top of the image is due to the C protective layer deposited during FIB preparation. High-Angle Annular Dark Field (HAADF) images of NC3 and NC4, taken after annealing, are shown in Figs. 3b and 3c, respectively. The surface topography of the NCs is conserved after annealing. However, zones of darker contrast at the interface with the buffer layer indicate the presence of voids in the NCs. The location of these voids below the surface bumps, indicates that the voids formed at the positions of the soft nano-rods. Higher resolution HAADF images of NC3 and NC4, containing one surface bump, are shown in Figs. 3d and 3g, respectively. Energy dispersive X-ray spectroscopy (EDX) chemical composition maps of the same regions, showing the distribution of Co and Pt, are shown in Figs. 3e,h and 3 f,i, respectively. Examination of these images indicates that in NC3, which has the narrowest nano-rods (width = 24 nm), Co atoms diffuse from the nano-rods into the hard magnetic matrix, remaining concentrated in a shell around the original interface with the nano-rods. On the other hand, in NC4, which has the widest nano-rods (width = 120 nm), diffusion of Co occurs mainly at the edges of the rods, with most of the nano-rod material remaining in place.

Chemical maps of the other concerned elements (Fe, Si, O), are shown in the Supplementary material (Figure S4), and Fe is also seen to be absent from the regions identified as voids. The formation of voids during annealing of our nano-composites is attributed to the Kirkendall effect [32,33]. Kirkendall established that atomic diffusion in substitutional solid solutions involves the diffusion of vacancies and that differences in the diffusion rates of different species across a bi-metal interface can result in movement of the interface and the formation of voids due to the coalescence of diffusing vacancies. While the Kirkendall effect is problematic when such voids deteriorate the strength of bonding between different metals (e.g., at welding joints), it is actually exploited to produce hollow nanostructures from chemically synthesised nanoparticles [32], including magnetic nanoparticles [34]. The position of the voids in the samples studied here indicates a higher rate of diffusion of Co and Fe atoms into FePt, compared to Pt diffusion into FeCo. This is in agreement with studies of intermixing in Fe-Pt multilayers [35]. In the present study, the formation of voids at the edges of the wide nano-rods in NC4 may be due to greater diffusion at the corners of nano-rods, leading to the edges serving as nucleation sites for vacancy precipitation. Alternatively, oxides have also been shown to serve as nucleation sites for vacancy precipitation [36], and

the formation of voids at the edges of nano-rods may also be due to oxidation of the side walls of the nano-rods which are not protected by Au during sample transfer. The almost complete disappearance of the nano-rods in NC3 may be explained by the closer proximity of the side walls which favours coalescence of voids from both sides, and a higher surface to volume ratio of the nano-rods, which favours diffusion between the rod and the matrix. It should also be noted that studies of Kirkendall void formation in nanoparticles had shown that void formation depends on the size of the nanoparticles [36], while interfacial strain is also proposed to play a role [33]. The observed concentration of Co atoms in a shell at the original nano-rod matrix interface may be due to limited diffusion time and/or a lower diffusivity of Co (and Fe) into ordered $L1_0$ FePt compared to the disordered A_0 phase [35], i.e., as the matrix becomes progressively more ordered during annealing, it gets harder for Co and Fe to diffuse into the matrix.

Diffusion between the hard and soft phases during sample fabrication may degrade the magnetic properties of the nanocomposite. Annealing of binary assemblies of bcc FeCo and fcc FePt chemically prepared nanoparticles (diameter = 6 nm) at 650 °C for 1 h was reported to lead to diffusion resulting in either partial or total dissolution of the FeCo nanoparticles in a $L1_0$-FeCoPt matrix [37]. Some diffusion was also reported following annealing at 700 °C for 20 min of nanocomposites consisting of Co nanoclusters (average diameter = 7.9 nm) coated in Fe/Pt bilayers [38]. In this case high Co content inclusions remained, while total interdiffusion occurred in Co/Fe/Pt multilayers with the same overall Co content treated to the same annealing conditions.

As a result of diffusion during the annealing step, which is necessary to form the hard magnetic $L1_0$FePt phase, the model architecture of the as-deposited NCs is modified. However, concentration of the diffused atoms in a shell at the original nano-rod matrix interface in the samples with the narrowest nano-rods, and limitation of diffusion to the edges of the widest nano-rods, ensures that the nanostructures of the annealed NCs are nevertheless relatively well defined. This allows us to study the influence of the original soft feature size on magnetisation reversal in these hard–soft nanocomposites. What is more, diffusion can be taken into consideration during micromagnetic modelling. In the discussion below about the magnetic properties, we will make the over-simplified assumption that the volume content of soft magnetic material in the NCs is equivalent to that of the corresponding as-fabricated NCs.
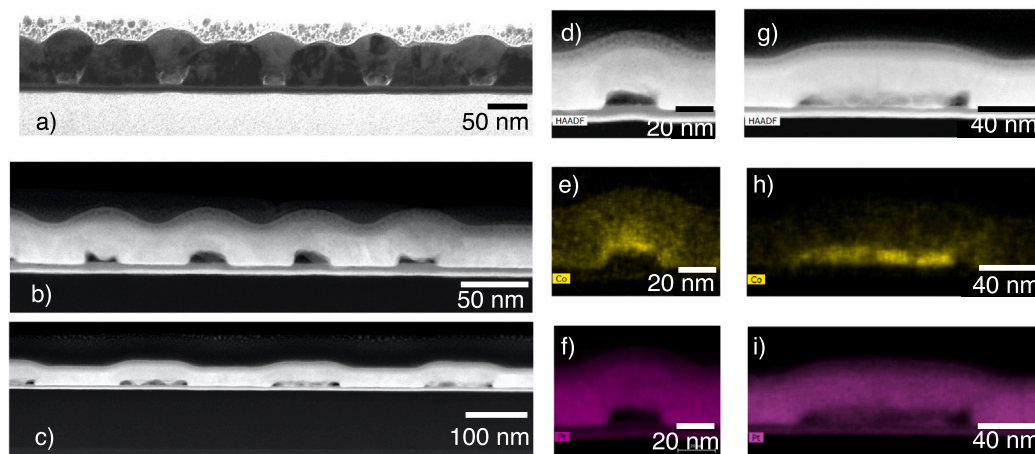
Fig. 3. TEM cross-sectional images: (a) NC2 before heat treatment (bright field mode), (b) & (d) NC3 and (c) & (g) NC4, after annealing (high-angle annular dark-field imaging mode), (e) & (f) NC3 and (h) & (i) NC4, compositional maps of Co and Pt.

3.2. Experimentally probed global magnetic properties

In-plane hysteresis loops of the four hard–soft NCs, measured with the field applied parallel to the long axis of the nano-rods are compared with an in-plane measurement on a reference array of hard FePt μ-pads in Fig. 4a (no demagnetising field corrections). The NCs present single magnetic phase behaviour without any obvious soft magnetic component. The M(H) loop of NC1, which has the lowest soft phase volume ratio (1.8%), is comparable to that of the reference array of hard FePt μ-pads. While the volume ratio of the soft phase is too low to expect any significant influence on remanence, it is noteworthy that the presence of nanoscale soft rods/shells in NC1, which could serve as nucleation sites for magnetisation reversal in the hard matrix, did not have any significant influence on coercivity. M(H) loops of the other hard–soft NCs are significantly modified with respect to that of the reference sample and the evolution in coercivity and remanence with soft phase content of the NCs is shown in Fig. 4b. The inverse behaviour of coercivity and remanence with increasing volume content of soft phase, classically seen in hard–soft nanocomposites, is also found here. Concerning the general shape of the M(H) curves, that of NC4 is seen to have the concave shape (most obvious in Fig. 4d) that Kneller and Hawig predicted for "an overaged microstructure", while those of the other samples have the "normal" convex shape they predicted for NCs with an optimum microstructure [2]. The in-plane M(H) loop of an FeCo (6 nm)/FePt (25 nm) bilayer prepared under the same conditions as the nanocomposites, is compared with those of the nanocomposites in the Supplementary material (Fig. S5). The much lower value of coercivity of the bilayer, despite the reduced thickness of it's soft magnetic layer (6 nm in the bilayer vs 10 nm in the NCs), shows the importance of controlling the size of the soft phase in more than one dimension. Nevertheless, the higher volume fraction of soft material in the bilayer (19%) also contributes to the lower value of coercivity.

To assess the potential impact of nano-rod shape anisotropy on magnetisation reversal, in-plane hysteresis curves measured with the applied field parallel and perpendicular to the long axis of NC2 (the sample with the highest demagnetising field factor) are compared in Fig. 4c. The similarity between the two curves indicates that the effect of shape anisotropy of the soft inclusions upon magnetisation reversal is negligible compared to the magnetocrystalline anisotropy of the non-textured hard magnetic matrix. To assess the potential influence of the topographical features induced in the hard matrix by depositing it on an array of nano-rods (indents on the bottom surface and associated bumps on the top surface), we fabricated an additional nanocomposite (NC4-Pt) consisting of non-magnetic Pt nano-rods in a hard magnetic FePt matrix with the same nano-rod dimensions as in NC4. Fig. 4d

shows that the M(H) loop of this sample is comparable to that of the reference FePt μ-pads but quite different to that of NC4. This confirms that the drop in coercivity in the soft-in-hard NCs is due to the soft magnetic nature of the nano-inclusions, rather than localised changes in demagnetising fields associated with the topographical features in the hard matrix.

Future directions of interest in this field include a more detailed study of the influence of the size and shape of soft inclusions (e.g., using First Order Reversal Curve measurements to study coupling between the hard and soft phases) as well as the impact of annealing conditions on diffusion and void formation.

3.3. Experimentally probed local magnetic properties

To probe the localised character of magnetisation reversal in our NCs, we carried out MFM imaging in the virgin state and then in different remanent states. A similar approach was used by Neu et al. to study magnetisation reversal in a micro-patterned SmCo$_5$/Fe/SmCo$_5$ trilayer nanocomposite [39]. The first column in Fig. 5 contains topographic images of an individual hard μ-pad and of individual soft-in-hard μ-pads from NC1, NC2, NC3 and NC4. The other columns contain MFM images in the virgin state and different remanent states, starting from an applied field pulse of +3T (except for the hard μ-pad) and then followed by successive application of negative field pulses of growing intensity (the magnetic field is applied in-plane along the long axis of the nano-rods, i.e., along the vertical axis of the image). The positions of the original nano-rods are clearly identified in the topographic images of the NCs, since the FePt deposit followed the topography imposed by the underlying nano-rods. The virgin state MFM images of all samples are comparable, having a fine granular structure that is typical of fine grained hard magnetic films [40]. The average size of individual magnetic features (100−200 nm) is greater than that of the average grain size of the FePt matrix phase (25 nm), which is indicative of exchange coupling between grains. A somewhat finer granular structure is also seen in the remanent state MFM images, most often together with one or two other types of magnetic contrast. One type, hereafter referred to as "edge contrast", is situated at the upper and lower edges of the reference hard and NC μ-pads, i.e., along the edges which are perpendicular to the direction of the applied magnetic field. The edge contrast, which is light at the upper edges and dark at the lower edges following application of a field pulse of +3 T, reflects the opposite sign of the z-component of the stray magnetic field signals produced above the μ-pads, by magnetic charges at these edges, following in-plane magnetisation. The edge contrast of all samples becomes weaker before practically disappearing after application of a field of −1 T. The field value of −1 T is close to the coercivity of the
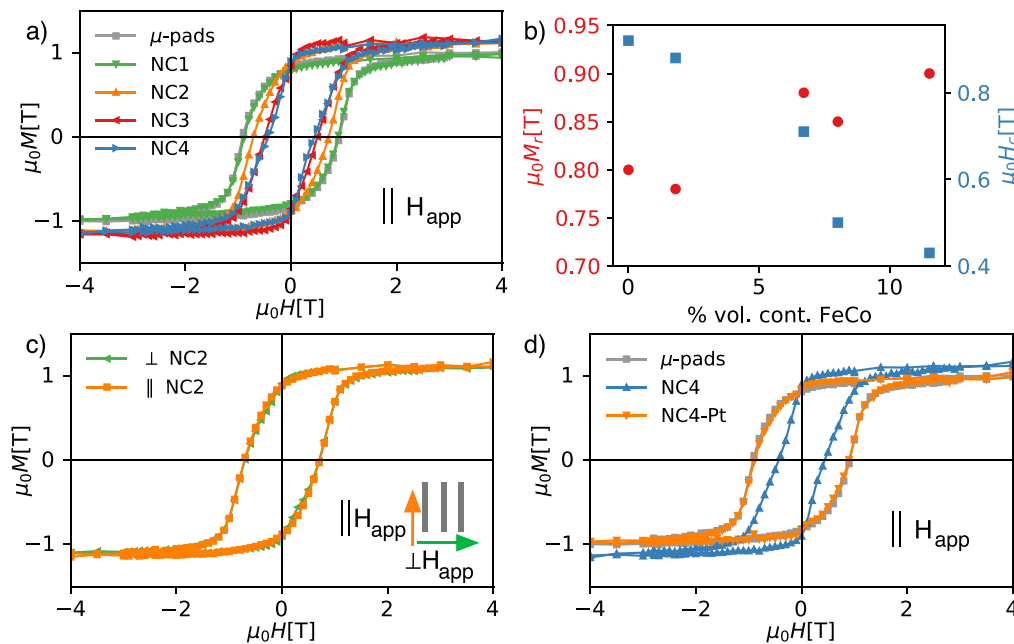
Fig. 4. (a) M(H) loops of FePt μ-pads and soft-in-hard nanocomposites (field applied in-plane and parallel to the long axis of the nano-rods), (b) Corresponding remanent magnetisation (μ_0M_r) and coercivity (μ_0H_c) as a function of FeCo volume content, (c) M(H) loops of NC2 with the in-plane field applied parallel or perpendicular to the long axis of the nano-rods, (d) M(H) loops of FePt μ-pads, NC4 and NC4-Pt (field applied in-plane and parallel to the long axis of the nano-rods).

hard micro-pads and NC1, while it is higher than that of NC2, NC3 and NC4. A reversed edge contrast of relatively high intensity is observed following application of a field of −3 T. The observed evolution in the edge contrast may be attributed to reversal of the edges of the hard matrix of all samples. As the edges of the nanocomposites are free of nano-rods, their reversal in NC2, NC3 and NC4 could be expected at an applied field of −1 T. In the case of NC2, NC3 and NC4, we can also see an additional fine contrast, which manifests itself as a periodic set of horizontal lines. The spacing of the lines is correlated with the length of the original underlying soft nano-rods (nano-shells in the case of diffused nano-rods). The periodic horizontal line contrast of NC2 and NC3 is not evident in the image taken after application of a field of −500 mT and it then reappears for higher negative fields. Based on the spacing of the lines and the field values at which the periodic horizontal line contrast of NC2, NC3 and NC4 are seen to switch, we associate the periodic fine contrast with the soft magnetic inclusions which are well-coupled (NC2 and NC3) or partially coupled (NC4) to the hard magnetic matrix. Finally, the absence of the periodic fine contrast in NC1 may be attributed to the fact that while the size of the individual nano-rods is the same in NC1 and NC3, their lower density in NC1 leads to them being camouflaged by the hard matrix.

3.4. Simulated magnetic properties

Micromagnetic simulations were performed to support our experimental analysis of the influence of the size, shape and volume fraction of soft magnetic or non-magnetic inclusions in a hard magnetic matrix, on magnetisation reversal. Three different sample architectures were modelled: "μ-pad" (L1$_0$ FePt alone), "ideal" (non-diffused FeCo or Pt nano-rods in a matrix of L1$_0$ FePt) and "diffused" (diffused FeCo nano-rods in a matrix of L1$_0$ FePt), as schematised in Fig. 6a. The same FePt matrix was used for all the simulated nanocomposites, varying only the size and distribution of the nano-rods, as listed in Table 2. These dimensions were estimated based on the analysis of TEM compositional maps (Fig. 3). In the finer structures (NC1, NC2 and NC3), diffusion is considered to lead to the transformation of the soft FeCo nano-rods into soft (FeCo)$_3$Pt nano-shells, resulting in the creation of voids at the original positions of the nano-rods. In the coarsest structure (NC4), the

Table 2
Outer dimensions of the voids and the diffused regions, according to the schematic shown in Fig. 6a. For NC4, voids were considered to be formed only at the sides edges of the original FeCo nano-rods, not on the their top edge.

Sample	w void	l void	t void	w diff	l diff	t diff
NC1	24	200	6	44	220	16
NC2	30	400	6	60	420	16
NC3	24	200	6	44	220	16
NC4	140	420	6	120	400	10

formation of voids at the edges of the soft nano-rod is considered. In all cases, voids are modelled as a nonmagnetic phase. The size of the FePt grains of the hard matrix was set at approximately 25 nm and an isotropic easy axes distribution was imposed. Neighbouring grains were in direct contact (no grain boundary phase) and perfectly coupled. Concerning the matrix, the literature value of magnetisation of L1$_0$ FePt ($\mu_0M_s = 1.43$ T) was assumed [41] while the anisotropy constant ($K_u = 2.88$ MJ/m^3), order parameter (S = 0.74), and exchange stiffness (A = 9.4 pJ/m) were deduced by adjusting the simulation parameters for a reference hard magnetic layer, so as to match the experimental hysteresis loop of our FePt μ-pads [42]. For the soft magnetic phases, the values considered for FeCo (J$_s$=2.0 T, A = 35 pJ/m, for Fe$_{40}$Co$_{60}$) and (FeCo)$_3$Pt (J$_s$ = 1.57 T, A = 20 pJ/m) were obtained from literature and experiments [43,44]. The finite element solver takes into account the following boundary and interface conditions. At the outer boundary of the magnet, the normal derivative of the magnetisation components is zero [45]. At materials interfaces, the products of the normal derivative of the magnetisation components with the local exchange constant is continuous [46]. In our finite element micromagnetic solver both conditions are taken into account [47].

Fig. 6a shows the respective geometries used for simulating the μ-pad, NC1-NC3 (fine) and NC4 (coarse) diffused nanocomposites, in plan-view, cross-section and perspective, together with the angular distribution of the matrix grains and the colour code for the constituent phases. Table 2 lists nano-rods dimensions for the non-magnetic (or void) and diffused components. For "ideal" model these dimensions are reported in Table 1. All the architectures are displayed in Figure S3 of Supplementary material. The simulated demagnetisation curves
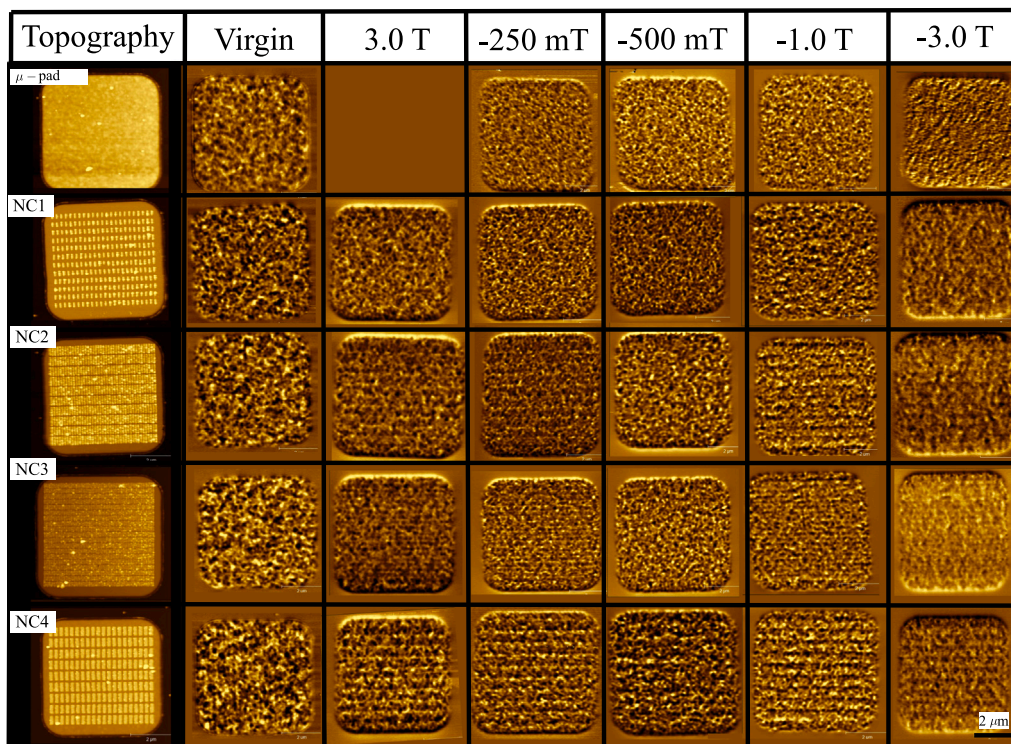
Fig. 5. ((First column) AFM topography images of a hard μ-pad and soft-in-hard nanocomposites. (All other columns) MFM phase contrast images in the virgin state and different remanent states following in-situ application of magnetic field pulses of different intensity and sign.
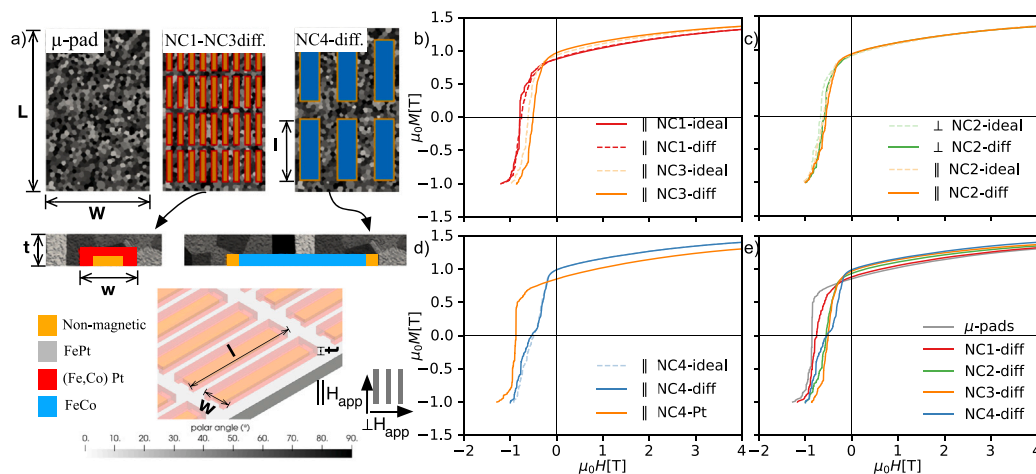

Fig. 6. (a) Schematics of the models used in micromagnetic simulations. The "diffused" (diff) model takes into account voids (non magnetic) formed due to diffusion during annealing. Simulated demagnetisation curves of (b) NC1 & NC3, (c) NC2, (d) NC4 & NC4-Pt and (e) FePt μ-pads & all soft-in-hard nanocomposites. The magnetic field is applied in-plane and parallel to the long axis of the nano-rods for all samples, field also applied perpendicular to the long axis of the nano-rods for NC2.).

of ideal and diffused soft-in-hard NCs are compared in Fig. 6b (NC1, NC3), 6c(NC2) and 6d (NC4), considering the applied magnetic field to be parallel to the long axes of the soft nano-rods. No significant difference is observed between the demagnetisation curves of the ideal and diffused versions of NC1 and NC4, which can be attributed to the low volume content of soft nano-rods in the former and the limited extent of diffusion in the latter. Diffusion leads to a small but observable drop in coercivity of 10% and 18% in NC2 and NC3, respectively. Demagnetisation curves of NC2, the sample containing nano-rods with the highest shape anisotropy, were also simulated considering the applied magnetic field to be perpendicular to the long axes of the soft nano-rods (Fig. 6c). In agreement with the corresponding experimental measurements shown in Fig. 4c, the shape anisotropy of the soft nano-rods

($\mu_0 H_c = 0.23$ T/0.15 T for ideal/diffused rods, calculated with non-magnetic matrix) does not influence the demagnetisation behaviour of the overall composite. The simulated demagnetisation curve of NC4-Pt, with non-magnetic nano-rods (Fig. 6d), is comparable to that of the reference hard magnetic matrix, while it is noticeably different to that of NC4, with magnetic nano-rods of the same size, in good agreement with the corresponding measurements (Fig. 4d). A comparison of the simulated demagnetisation curves of diffused soft-in-hard NCs (Fig. 6e) reveals the same trend observed in measurements (Fig. 4a) and the absolute values of coercivity and remanence are comparable. The size of the soft nano-rods is seen to influence the general shape of the simulated demagnetisation curves, with that of NC4 being somewhat concave (most obvious in Fig. 6d), in relatively good agreement with
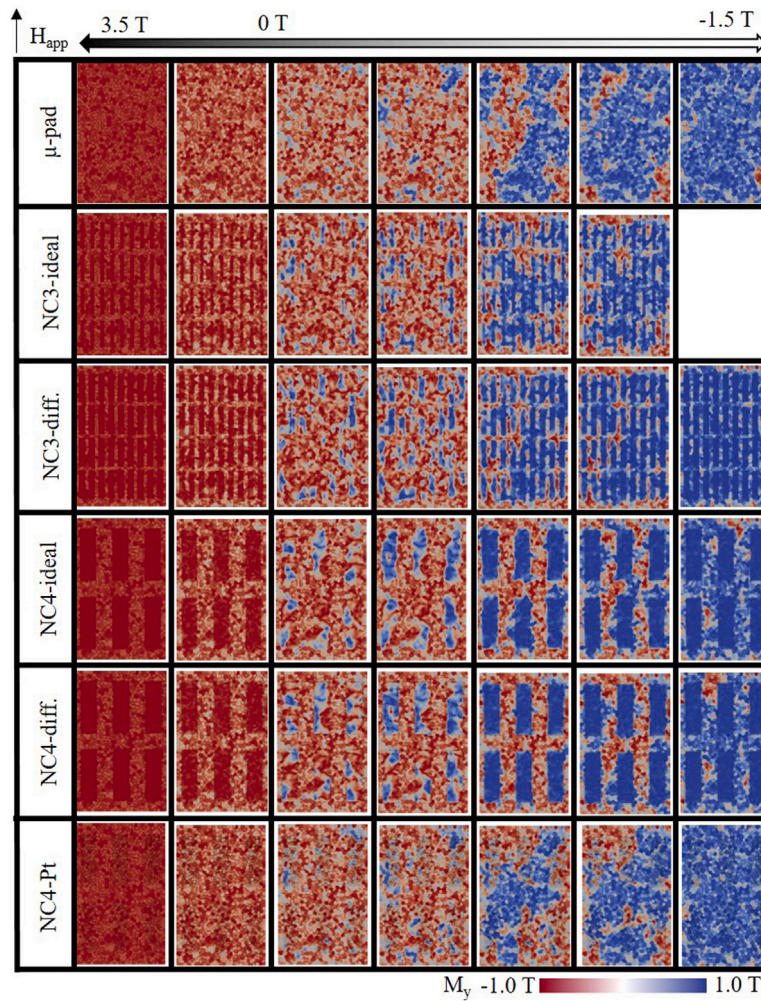
Fig. 7. Snapshots of simulated magnetisation distribution maps of select samples, at a height of 8 nm above the buffer layer, taken at different field values along the demagnetising curves (the applied magnetic field is in-plane and parallel to the long axis of the nano-rods).

the experimental measurements (Fig. 4e) and the predictions of Kneller and Harwig [2]. The demagnetisation curves presented in Fig. 6 were calculated by applying a preconditioned conjugate gradient method minimising the Gibbs free energy. The observed zig-zag fluctuations are indicative of the domain reversal processes occurring in a certain number of grains at each step of energy minimisation, which corresponds to different applied magnetic fields. This phenomenon closely resembles the Barkhausen effect and can be attributed to the relatively limited number of grains (a total of 1500) incorporated within our simulation model. This granularity in the model leads to the stepwise changes in magnetisation observed as zig-zag patterns in the M-H curves.

Snapshots of simulated magnetisation distribution maps taken from along the demagnetising curves of a hard magnetic μ-pad, NC3 (ideal and diffused), NC4 (ideal and diffused) and NC4-Pt are compared in Fig. 7. The applied magnetic field is parallel to the long axis of the nano-rods, and the contrast and colour are directly proportional to the intensity and direction of magnetisation, respectively, at a height of 8 nm above the buffer layer. These images are not directly comparable with the MFM images shown in Fig. 5, which reflect changes in the stray field patterns produced above the samples, in different remanent states. Besides, the surface area considered is smaller because of limitations due to the time and computing power needed to perform the simulations. Nevertheless, these snapshots provide further evidence on how the size and nature of the inclusions together with diffusion affect magnetisation reversal in the studied samples. Magnetisation reversal is clearly seen to initiate within the soft inclusions of the soft-in-hard

NCs, while it starts in multiple, randomly positioned regions in the hard μ-pad and in the NC with non-magnetic inclusions. Reversal proceeds in a similar manner in the latter two samples, through growth and then coalescence of reversed domains. In the case of NC4, reversal is practically complete within the soft inclusions before it proceeds in the hard matrix, and there are only negligible differences between the ideal and diffused cases. On the other hand, in the case of NC3, there is a discernible difference between the ideal and diffused cases. Reversal of the hard matrix starts before complete reversal of the soft inclusions in the ideal case, indicative of good coupling between the two phases. Soft inclusions in the diffused case of NC3 are more distinct during reversal, which is attributed to their relatively bigger dimensions and thus somewhat poorer coupling with the hard matrix.

4. Conclusions and prospects

A combination of e-beam lithography, evaporation, sputtering and lift-off has been successfully exploited to fabricate highly regular repeat arrays of FeCo soft magnetic nano-rods embedded in chemically disordered (i.e., magnetically soft) FePt μ-pads, across mm-sized substrates. Annealing to transform these into soft-in-hard nano-composites through chemical ordering of the FePt μ-pads, led to the formation of nano-scale Kirkendall voids. In the sample with the widest rods (w = 120 nm), the voids are seen to form at the edges of the rods, while in a sample with the narrowest rods (w = 24 nm), the original rods are practically replaced by the voids. In the latter case, the expelled Co

atoms are seen to accumulate in a shell surrounding the original rod, thus maintaining a composite structure, notwithstanding the undesired diffusion and void formation. The high degree of control achieved over the nanostructures studied here, despite changes induced by diffusion during annealing, render them as model soft–hard nanocomposites. Indeed, the very regular nature of the nanocomposite structure greatly facilitates the observation of Kirkendall nano-voids, which could be expected to form in hard–soft nanocomposites fabricated by other methods, but which may go undetected. More importantly, the high degree of control over the nanostructure facilities interpretation of results from localised magnetic characterisation and narrows the gap between the physical nanostructure (both the idealised and real versions) and the sample architectures used in micromagnetic simulations of magnetisation reversal. The important results from experimental magnetic measurements are quantitatively supported by micromagnetic simulations, namely (1) a low density of soft magnetic FeCo nano-inclusions (shells) does not affect magnetisation reversal in the $L1_0$ FePt hard matrix, (2) increasing the density or the density and size (width) of the soft nano-inclusions leads to a decrease in coercivity and concomitant increase in remanent magnetisation of the nanocomposite, (3) increasing the size (width) of the soft nano-inclusions leads to a cross over from convex to concave demagnetising curves, which can be attributed to poorer inter-phase coupling, (4) the shape anisotropy of the soft magnetic inclusions does not infer any shape anisotropy on the nanocomposites and (5) changes in the topography of the matrix alone do not affect magnetisation reversal, i.e., it is the soft magnetic nature of the inclusions in the soft-in-hard nanocomposites that affects magnetisation reversal. Thanks to the very good agreement between experiments and simulations, the micromagnetic modelling approach can be used for in-silico optimisation of soft-in-hard nanocomposites, through a tuning of the dimensions, shape, spatial distribution and volume content of the soft phase. Iterations between the optimised simulated model structures and nanofabricated model samples can be used to quantitatively investigate the critical parameters for developing soft–hard magnetic nanocomposites. Future directions of interest in this field include a more detailed study of the influence of the size and shape of soft inclusions as well as the impact of annealing conditions on diffusion and void formation. Other combinations of soft and hard magnetic materials, including high magnetisation $Fe_{60}Co_{40}$ and high anisotropy rare earth transition metal phases, could also be considered. Beyond serving as model systems to study magnetisation reversal, one could imagine developing such nanocomposites for use in nano-devices. In this case, once the dimensions and disposition of the soft inclusions have been optimised, they could be fabricated by the much faster and upscalable technique of nanoimprint lithography.

CRediT authorship contribution statement

Isabelle G. de Moraes: Conceptualization, Data curation, Formal analysis, Funding acquisition, Investigation, Methodology, Validation, Visualization, Writing – original draft, Writing – review & editing. **Johann Fischbacher:** Conceptualization, Formal analysis, Investigation, Methodology, Software, Validation, Visualization, Writing – original draft, Writing – review & editing. **Yuan Hong:** Conceptualization, Data curation, Formal analysis, Funding acquisition, Investigation, Methodology, Validation, Visualization, Writing – review & editing. **Cécile Naud:** Conceptualization, Methodology, Validation, Writing – original draft. **Hanako Okuno:** Data curation, Methodology, Validation, Writing – original draft. **Aurelien Masseboeuf:** Data curation, Validation, Visualization, Writing – original draft, Funding acquisition. **Thibaut Devillers:** Conceptualization, Data curation, Formal analysis, Funding acquisition, Methodology, Project administration, Supervision, Validation, Visualization, Writing – original draft, Writing – review & editing. **Thomas Schrefl:** Conceptualization, Data curation, Formal analysis, Funding acquisition, Methodology, Project administration, Software, Validation, Visualization, Writing – original draft, Writing – review

& editing, Supervision. **Nora M. Dempsey:** Conceptualization, Formal analysis, Funding acquisition, Project administration, Resources, Supervision, Validation, Writing – original draft, Writing – review & editing.

Declaration of competing interest

The authors declare that they have no known competing financial interests or personal relationships that could have appeared to influence the work reported in this paper.

Acknowledgements

Appendix A. Supplementary data

Supplementary material related to this article can be found online at https://doi.org/10.1016/j.actamat.2024.119970.

References

[1] R. Coehoorn, D. De Mooij, C.d. de Waard, Meltspun permanent magnet materials containing Fe3B as the main phase, J. Magn. Magn. Mater. 80 (1) (1989) 101–104.

[2] E.F. Kneller, R. Hawig, The exchange-spring magnet: A new material principle for permanent magnets, IEEE Trans. Magn. 27 (4) (1991) 3560–3588.

[3] R. Horikawa, H. Fukunaga, M. Nakano, T. Yanai, Magnetic properties of isotropic and anisotropic SmCo5/α-Fe nanocomposite magnets with a layered structure simulated by micromagnetic theory, J. Appl. Phys. 115 (17) (2014).

[4] R. Skomski, J. Coey, Giant energy product in nanostructured two-phase magnets, Phys. Rev. B 48 (21) (1993) 15812.

[5] S. Bance, H. Oezelt, T. Schrefl, M. Winklhofer, G. Hrkac, G. Zimanyi, O. Gutfleisch, R. Evans, R. Chantrell, T. Shoji, et al., High energy product in battenberg structured magnets, Appl. Phys. Lett. 105 (19) (2014).

[6] A. López-Ortega, M. Estrader, G. Salazar-Alvarez, A.G. Roca, J. Nogués, Applications of exchange coupled bi-magnetic hard/soft and soft/hard magnetic core/shell nanoparticles, Phys. Rep. 553 (2015) 1–32.

[7] H. Zeng, J. Li, J.P. Liu, Z.L. Wang, S. Sun, Exchange-coupled nanocomposite magnets by nanoparticle self-assembly, Nature 420 (6914) (2002) 395–398.

[8] B. Shen, A. Mendoza-Garcia, S.E. Baker, S.K. McCall, C. Yu, L. Wu, S. Sun, Stabilizing Fe nanoparticles in the SmCo5 matrix, Nano Lett. 17 (9) (2017) 5695–5698.

[9] I. de Moraes, N.M. Dempsey, Nanocomposites for permanent magnets, in: New Trends in Nanoparticle Magnetism, Springer, 2021, pp. 403–433.

[10] M. Yue, X. Zhang, J.P. Liu, Fabrication of bulk nanostructured permanent magnets with high energy density: Challenges and approaches, Nanoscale 9 (11) (2017) 3674–3697.

[11] W. Li, H. Sepehri-Amin, L. Zheng, B. Cui, A. Gabay, K. Hono, W. Huang, C. Ni, G. Hadjipanayis, Effect of ball-milling surfactants on the interface chemistry in hot-compacted SmCo5 magnets, Acta Mater. 60 (19) (2012) 6685–6691.

[12] J.P. Liu, E. Fullerton, O. Gutfleisch, D.J. Sellmyer, Nanoscale Magnetic Materials and Applications, Springer, 2009.

[13] Q. Geng, L. Yao, Q. Zheng, P. Si, B. Bian, J. Du, Effect of soft magnetic phase addition on the microstructure and properties of SmCo5/FeCo anisotropic nanocomposite powders, J. Magn. Magn. Mater. 553 (2022) 169296, http://dx.doi.org/10.1016/j.jmmm.2022.169296.

[14] H. Sepehri-Amin, I. Dirba, X. Tang, T. Ohkubo, T. Schrefl, O. Gutfleisch, K. Hono, Development of high coercivity anisotropic Nd-Fe-B/Fe nanocomposite powder using hydrogenation disproportionation desorption recombination process, Acta Mater. 175 (2019) 276–285, http://dx.doi.org/10.1016/j.actamat.2019.06.017.

[15] S.M. Parhofer, J. Wecker, C. Kuhrt, G. Gieres, L. Schultz, Remanence enhancement due to exchange coupling in multilayers of hard-and softmagnetic phases, IEEE Trans. Magn. 32 (5) (1996) 4437–4439.

[16] J.P. Liu, Y. Liu, R. Skomski, D.J. Sellmyer, High energy products in exchange-coupled nanocomposite films, IEEE Trans. Magn. 35 (5) (1999) 3241–3246.

[17] E.E. Fullerton, J. Jiang, S. Bader, Hard/soft magnetic heterostructures: Model exchange-spring magnets, J. Magn. Magn. Mater. 200 (1–3) (1999) 392–404.

[18] T. Seki, Y. Takahashi, K. Hono, Magnetic properties and microstructure of the granular films processed by annealing FePt-based multilayers, IEEE Trans. Magn. 41 (10) (2005) 3799–3801.

[19] V. Neu, S. Sawatzki, M. Kopte, C. Mickel, L. Schultz, Fully epitaxial, exchange coupled SmCo$_5$ /Fe multilayers with energy densities above 400 kJ/m^3, IEEE Trans. Magn. 48 (11) (2012) 3599–3602.

[20] W.B. Cui, H. Sepehri-Amin, Y. Takahashi, K. Hono, Hard magnetic properties of spacer-layer-tuned NdFeB-Ta-Fe nanocomposite films, Acta Mater. 84 (2015) 405–412.

[21] K. Son, G. Schütz, E. Goering, Effect of the soft layer thickness on magnetization reversal process of exchange-spring nanomagnet patterns, Curr. Appl. Phys. 20 (4) (2020) 477–483.

[22] K. Son, G. Schütz, Fabrication and temperature-dependent magnetic properties of large-area L10-FePt/Co exchange-spring magnet nanopatterns, Physica E 115 (2020) 113687.

[23] R. Skomski, P. Manchanda, I. Takeuchi, J. Cui, Geometry dependence of magnetization reversal in nanocomposite alloys, JOM 66 (2014) 1144–1150.

[24] T. Groves, Electron beam lithography, in: Nanolithography, Elsevier, 2014, pp. 80–115.

[25] Y. Hong, I. de Moraes, G.G. Eslava, S. Grenier, E. Bellet-Amalric, A. Dias, M. Bonfim, L. Ranno, T. Devillers, N.M. Dempsey, A high throughput study of both compositionally graded and homogeneous Fe–Pt thin films, J. Mater. Res. Technol. 18 (2022) 1245–1255.

[26] L. Exl, J. Fischbacher, A. Kovacs, H. Oezelt, M. Gusenbauer, T. Schrefl, Preconditioned nonlinear conjugate gradient method for micromagnetic energy minimization, Comput. Phys. Comm. 235 (2019) 179–186.

[27] R. Quey, P. Dawson, F. Barbe, Large-scale 3D random polycrystals for the finite element method: Generation, meshing and remeshing, Comput. Methods Appl. Mech. Engrg. 200 (17–20) (2011) 1729–1745.

[28] R. Quey, Neper, URL https://neper.info/.

[29] Salome, Salome, URL https://www.salome-platform.org/.

[30] D. Systèmes, 3D precise mesh, URL https://www.spatial.com/products/3d-precise-mesh.

[31] Q. Chen, A. Konrad, A review of finite element open boundary techniques for static and quasi-static electromagnetic field problems, IEEE Trans. Magn. 33 (1) (1997) 663–676.

[32] H.J. Fan, U. Gösele, M. Zacharias, Formation of nanotubes and hollow nanoparticles based on Kirkendall and diffusion processes: A review, small 3 (10) (2007) 1660–1671.

[33] J.G. Railsback, A.C. Johnston-Peck, J. Wang, J.B. Tracy, Size-dependent nanoscale Kirkendall effect during the oxidation of nickel nanoparticles, ACS Nano 4 (4) (2010) 1913–1920.

[34] J. Gao, G. Liang, B. Zhang, Y. Kuang, X. Zhang, B. Xu, FePt@ CoS2 yolk- shell nanocrystals as a potent agent to kill HeLa cells, J. Am. Chem. Soc. 129 (5) (2007) 1428–1433.

[35] T. Kaiser, W. Sigle, D. Goll, N. Goo, V. Srot, P. Van Aken, E. Detemple, W. Jäger, Transmission electron microscopy study of the intermixing of Fe–Pt multilayers, J. Appl. Phys. 103 (6) (2008).

[36] R. Resnick, L. Seigle, Nucleation of voids in metals during diffusion and creep, JOM 9 (1957) 87–94.

[37] M. Pousthomis, C. Garnero, C. Marcelot, T. Blon, S. Cayez, C. Cassignol, V. Du, M. Krispin, R. Arenal, K. Soulantica, et al., On the advantages of spring magnets compared to pure FePt: Strategy for rare-earth free permanent magnets following a bottom-up approach, J. Magn. Magn. Mater. 424 (2017) 304–313.

[38] C. Paleo, V. Dupuis, F. Wilhelm, A. Rogalev, O. Proux, O. Boisron, I. Kieffer, T. Epicier, M. Bugnet, D. Le Roy, Interplay between local structure and magnetic properties of graded exchange-coupled Co@ FePt nanocomposite films, Phys. Rev. B 102 (22) (2020) 224409.

[39] V. Neu, S. Zimmermann, S. Sawatzki, I. Monch, L. Schultz, Imaging the magnetization processes in epitaxial exchange coupled SmCo _{5} /Fe/Smco _{5} trilayers, IEEE Trans. Magn. 48 (11) (2012) 3644–3647.

[40] G. Ciuta, F. Dumas-Bouchiat, N.M. Dempsey, O. Fruchart, Some aspects of magnetic force microscopy of hard magnetic films, IEEE Trans. Magn. 52 (9) (2016) 1–8.

[41] J. Wang, H. Sepehri-Amin, Y. Takahashi, S. Okamoto, S. Kasai, J. Kim, T. Schrefl, K. Hono, Magnetization reversal of FePt based exchange coupled composite media, Acta Mater. 111 (2016) 47–55.

[42] S. Okamoto, N. Kikuchi, O. Kitakami, T. Miyazaki, Y. Shimada, K. Fukamichi, Chemical-order-dependent magnetic anisotropy and exchange stiffness constant of FePt (001) epitaxial films, Phys. Rev. B 66 (2) (2002) 024413.

[43] C. Mathieu, H.-J. Liu, K.S. Buchanan, V.R. Inturi, Volume exchange in soft FeCo films of high magnetization, J. Appl. Phys. 111 (7) (2012).

[44] M. Nahid, T. Suzuki, Magnetic properties and structure of (FeCo) 3 Pt thin films, J. Appl. Phys. 95 (11) (2004) 7160–7162.

[45] Brown, W.F., Micromagnetics, in: Interscience tracts on physics and astronomy, Interscience Publishers, 1963.

[46] H. Kronmüller, H. Hilzinger, Incoherent nucleation of reversed domains in Co5Sm permanent magnets, J. Magn. Magn. Mater. 2 (1) (1975) 3–10.

[47] T. Schrefl, G. Hrkac, S. Bance, D. Suess, O. Ertl, J. Fidler, Numerical methods in micromagnetics (finite element method), in: Handbook of Magnetism and Advanced Magnetic Materials, Wiley Online Library, 2007.